The Astrophysical Journal, 954:43 (11pp), 2023 September 1 https://doi.org/10.3847/1538-4357/ace7be

Suprathermal Electron Transport and Electron Beam Formation in the Solar Corona

Bofeng Tang[1,2], Haihong Che[1,2], Gary P. Zank[1,2], and Vladimir I. Kolobov[2,3]
[1] Department of Space Science, University of Alabama in Huntsville, Huntsville, AL 35899, USA
[2] Center for Space Plasma and Aeronomic Research (CSPAR), University of Alabama in Huntsville, Huntsville, AL 35899, USA
[3] CFD Research Corporation, Huntsville, AL 35806, USA
Received 2023 February 15; revised 2023 July 3; accepted 2023 July 14; published 2023 August 22

Abstract

Electron beams that are commonly observed in the corona were discovered to be associated with solar flares. These "coronal" electron beams are found $\geqslant$300 Mm above the acceleration region and have velocities ranging from 0.1c up to 0.6c. However, the mechanism for producing these beams remains unclear. In this paper, we use kinetic transport theory to investigate how isotropic suprathermal energetic electrons escaping from the acceleration region of flares are transported upwardly along the magnetic field lines of flares to develop coronal electron beams. We find that magnetic focusing can suppress the diffusion of Coulomb collisions and background turbulence and sharply collimate the suprathermal electron distribution into beams with the observed velocity within the observed distance. A higher bulk velocity is produced if energetic electrons have harder energy spectra or travel along a more rapidly expanding coronal magnetic field. By modeling the observed velocity and location distributions of coronal electron beams, we predict that the temperature of acceleration regions ranges from 5×10^6 to 2×10^7 K. Our model also indicates that the acceleration region may have a boundary where the temperature abruptly decreases so that the electron beam velocity can become more than triple (even up to 10 times) the background thermal velocity and produce the coronal type III radio bursts.

Unified Astronomy Thesaurus concepts: Solar corona (1483)

1. Introduction

Solar type III radio bursts, first discovered by Wild & McCready (1950), are believed to be produced by electron beams via an electron two-stream instability (ETSI; Ginzburg & Zhelezniakov 1958). Since then, type III radio bursts have been considered as a direct indicator of the existence of electron beams. Type III radio bursts include coronal and interplanetary bursts (Reid & Ratcliffe 2014). Coronal type III bursts are produced by electron beams within the solar corona, while interplanetary bursts are produced by the escape of energetic electrons into space, most of which can reach 1 au. In recent years, a large number of coronal type III radio bursts have been discovered. Some were associated with regular solar flares, but most were found to be associated with nanoflares (Thejappa et al. 1990; Saint-Hilaire et al. 2012). Nanoflares occur in the quiet Sun at a rate of 1 million events s^{-1} over the whole Sun (Aschwanden & Parnell 2002). These observations indicate that electron beams are commonly and frequently produced within the solar corona. In this paper, we use the term "coronal electron beams" to refer specifically to those electron beams associated with nanoflares and coronal type III radio bursts within the solar corona. These electron beams are related to particle acceleration and heating in the solar corona and probably contribute to the formation of the electron halo in the solar wind (Che & Goldstein 2014; Che et al. 2019). However, how so many coronal electron beams are generally produced in the corona is poorly understood and has not attracted sufficient attention.

Observations show that coronal electron beams originate from the escape of suprathermal electrons in the acceleration region of solar flares (Chen et al. 2013). Coronal type III radio bursts (a consequence of the presence of coronal electron beams) have typically been found at heights of $\geqslant$300 Mm (0.4 solar radii) above the photosphere (Morimoto 1961; Mercier & Rosenberg 1974; Reid & Kontar 2018a). These observations suggest that suprathermal electrons escape from the acceleration region of flares and form coronal electron beams after propagating upward over a certain distance. A schematic of the possible process that we advocate is shown in Figure 1. Theories suggest that an electron beam can trigger an ETSI that then produces type III radio bursts if the beam velocity is larger than the background electron thermal velocity (Che 2016). Suprathermal energetic electrons are accelerated during solar flares and usually do not carry a significant bulk momentum even in those cases where electron jets are produced. The jet velocity is commonly less than the local thermal speed due to intense plasma heating in the acceleration region (Che et al. 2021). Therefore, the formation of coronal electron beams from suprathermal electrons might be as illustrated in Figure 1. Initially, suprathermal electrons accelerate during solar flare eruptions in the low corona and collectively possess a zero or low bulk velocity, which is insufficient to trigger ETSI. Some energetic electrons then escape from the acceleration region and propagate upward along the magnetic field lines of flares. During their outward propagation, these suprathermal electrons with an initially random velocity distribution develop electron beams, and the bulk velocity rapidly increases enough to trigger the ETSI.

What effects commonly govern coronal electron beam formation is unclear. Observations of coronal type III radio bursts impose restrictions on the candidate mechanism. First, the mechanism producing coronal electron beams is independent of solar flares and can occur in the general plasma condition of the corona, since the electron beams form outside the acceleration region. Second, the mechanism can produce

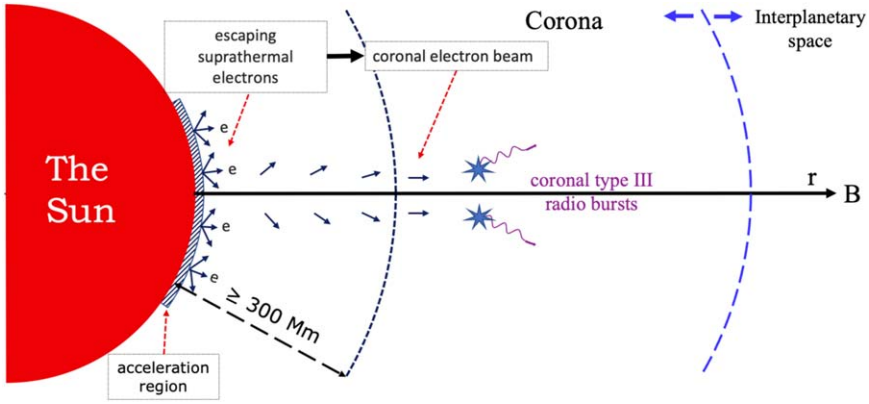

Figure 1. Schematic illustration of suprathermal electron transport and coronal electron beam formation inside the solar corona along a radial magnetic field. Initially, suprathermal electrons are accelerated during a solar flare eruption in the low corona. After the suprathermal electrons propagate upward several hundred megameters away from the acceleration region, coronal electron beams form due to magnetic focusing. These coronal electron beams have high bulk velocities and, therefore, can trigger ETSI and produce coronal type III radio bursts.

coronal electron beams within a minimum distance of ~300 Mm. That requires that the mechanism be very efficient in increasing the bulk velocity of the electrons shortly after they begin to propagate. Third, the ratio of the bulk velocity of some coronal electron beams to the local background electron thermal velocity can reach the threshold of ETSI but remain stable. Observations show that the bulk velocities of some coronal electron beams can reach up to 10 times the background electron thermal velocity (Krucker et al. 2007; Reid et al. 2011; Benz 2012, 2017; Chen et al. 2013, 2018), which is much larger than the threshold of the ETSI. It is unclear why these coronal beams achieve such high velocities without triggering ETSI. Previous studies of electron beams focused on the maintenance of the electron beams after triggering type III radio bursts in the solar corona and interplanetary space (Ergun et al. 1998; Li et al. 2006; Reid et al. 2011). However, what mechanism governs the coronal electron beam formation prior to triggering coronal type III radio bursts is not addressed.

A parallel sunward electric field is desirable to develop beams directly. However, beyond the acceleration region, i.e., far from the diffusion region of magnetic reconnection (MR), the plasma becomes nearly neutral and is usually described by magnetodynamics. Therefore, it is theoretically unexpected that a large-scale parallel electric field is commonly produced (Eyink et al. 2013; Beresnyak 2016; Kowal et al. 2017) and unlikely that it can be responsible for the formation of electron beams. Moreover, direct parallel electric field acceleration has been ruled out by the latest PSP observations in the area away from the acceleration region (Desai et al. 2022).

During propagation, besides a parallel electric field, suprathermal electrons experience three other possible effects, these being magnetic focusing (adiabatic focusing[4]), Coulomb collisions, and scattering by background turbulence. While the latter two effects diffuse the beams, magnetic focusing is the only remaining effect that allows for the development of electron beams. Magnetic focusing effectively transfers the perpendicular momentum to the parallel direction and collimates the suprathermal electrons propagating upward along the magnetic field line of flares (Tang et al. 2023). However, whether magnetic focusing can overcome diffuse effects and is sufficient to form coronal electron beams that trigger coronal type III radio bursts has yet to be established.

In this paper, we investigate the competition of these three effects in mediating the transport of suprathermal electrons and the formation of coronal electron beams within the solar corona. We show that magnetic focusing can suppress Coulomb collisions and turbulent scattering, leading to the formation of coronal electron beams. As a result, coronal electron beams develop and form efficiently from suprathermal electrons over the requisite observational distance (i.e., $\geqslant$300 Mm above the photosphere). Their bulk velocity can reach a saturated speed larger than the ETSI threshold and produce coronal type III radio bursts. Over this observation-constrained distance, the specific spatial configuration of the magnetic field of flares has little effect on the formation of coronal electron beams. Moreover, using a group of observed velocity and location distributions of coronal electron beams, our model predicts that the temperature of the flare acceleration regions ranges from 5×10^6 to 2×10^7 K. The coronal electron beam velocities range from $0.1c$ to $\sim 0.6c$ for locations from 400 to 700 Mm above the acceleration region, which is well consistent with the observations. Our model also suggests that the acceleration region may have a boundary where the temperature decreases. As a result, the bulk velocity of coronal electron beams can abruptly reach more than triple (even up to 10 times) the coronal background thermal velocity and produce coronal type III radio bursts; this explains the origin of electron beams with velocities up to 10 times the thermal velocity. In this paper, we only consider the formation of high bulk velocity coronal electron beams that can trigger a strong ETSI and produce coronal type III radio bursts. The generation of Langmuir waves and the maintenance of interplanetary electron beams after producing coronal type III radio bursts are beyond the scope of this paper.

This paper is organized as follows. In Section 2, we describe the electron transport model. The effect of the spatial structure of the magnetic field of flares on the form of the transport equation is emphasized. The specific forms for Coulomb and whistler turbulence scattering are introduced into the transport equation thereafter. Section 3 presents numerical solutions for the transport of suprathermal energetic electrons in the corona, showing how coronal electron beams form. Finally, conclusions and discussions are given in Section 4.

[4] Magnetic focusing is also called adiabatic focusing. We refer to it as magnetic focusing to emphasize that it is an effect of the magnetic field that changes with the spatial structure of the magnetic field. Magnetic focusing emerges naturally in deriving transport Equation (5) in the presence of a radial magnetic field and transport Equation (11) with a dipole field in Section 2.

2. Theoretical Model

2.1. Electron Transport Equation

The general form of the gyrophase averaged kinetic transport equation for a gyrotropic electron distribution function $f(\boldsymbol{x}, v, \mu, t)$ without a parallel electric field is given in Zank (2014),

$$\begin{aligned}&\frac{\partial f}{\partial t}+(v\mu\boldsymbol{b}+\boldsymbol{U})\cdot\nabla f\\&+\left[\left(-\frac{\partial \boldsymbol{U}}{\partial t}-\boldsymbol{U}\cdot\nabla\boldsymbol{U}\right)\cdot\boldsymbol{b}\frac{\mu}{v}-\frac{1-\mu^2}{2}\nabla\cdot\boldsymbol{U}\right)\\&-\frac{3\mu^2-1}{2}\boldsymbol{b}\cdot\nabla\boldsymbol{U}\cdot\boldsymbol{b}\Bigg]v\frac{\partial f}{\partial v}\\&+\frac{1-\mu^2}{2}[v\nabla\cdot\boldsymbol{b}+\mu\nabla\cdot\boldsymbol{U}\\&-\left(\left(\frac{\partial \boldsymbol{U}}{\partial t}+\boldsymbol{U}\cdot\nabla\boldsymbol{U}\right)\cdot\boldsymbol{b}\frac{2}{v}-3\mu\boldsymbol{b}\cdot\nabla\boldsymbol{U}\cdot\boldsymbol{b}\right]\frac{\partial f}{\partial\mu}\\&=\left(\frac{\delta f}{\delta t}\right)_{\rm sc},\end{aligned}\tag{1}$$

where $\boldsymbol{x}$ is the position in the rest frame; (v, μ) is the velocity magnitude and the cosine of the pitch angle measured in a moving frame of $\boldsymbol{U}=c(\boldsymbol{E}\times\boldsymbol{B})/B^2+U_{\parallel}\boldsymbol{b}$ with respect to the rest frame of the Sun; $U_{\parallel}=\boldsymbol{U}\cdot\boldsymbol{b}$, $\boldsymbol{E}$, and $\boldsymbol{B}$ are the external fields; $\boldsymbol{b}\equiv\boldsymbol{B}/B$ is the unit vector along the magnetic field; and $(\delta f/\delta t)_{\rm sc}$ is the scattering term.

In a frame moving with a constant velocity $\boldsymbol{U}=U\boldsymbol{b}$ along the magnetic field, $\nabla\cdot\boldsymbol{U}=U\nabla\cdot\boldsymbol{b}$, and the divergence of $\boldsymbol{b}$ can be expressed in terms of the magnetic field $\boldsymbol{B}$,

$$\nabla\cdot\boldsymbol{b}=-\frac{\boldsymbol{B}\cdot\nabla B}{B^2},\tag{2}$$

using $\nabla\cdot\boldsymbol{B}=0$. The velocity v of electrons is always much larger than the plasma background velocity U, i.e., $U\ll v$, making it safe to ignore U. Therefore, transport Equation (1) reduces to

$$\frac{\partial f}{\partial t}+v\mu\boldsymbol{b}\cdot\nabla f-\frac{v(1-\mu^2)}{2}\frac{\boldsymbol{B}\cdot\nabla B}{B^2}\frac{\partial f}{\partial\mu}=\left(\frac{\delta f}{\delta t}\right)_{\rm sc}.\tag{3}$$

In practical applications, the detailed expression of transport Equation (3) depends on the magnetic field $\boldsymbol{B}$ and the scattering term $(\delta f/\delta t)_{\rm sc}$. The second and third terms associated with $\boldsymbol{B}$ on the left-hand side reflect the effect of magnetic focusing. In a global spherical coordinate system whose origin is the center of the Sun, the magnetic field has the form of $\boldsymbol{B}=B_r\hat{e}_r+B_\theta\hat{e}_\theta+B_\phi\hat{e}_\phi$, where $\hat{e}_r$, $\hat{e}_\theta$, and $\hat{e}_\phi$ are the radial, polar, and azimuthal unit vectors, respectively. In this paper, we consider two spatial forms for the magnetic field: a radial magnetic field ($\boldsymbol{B}\approx B_r\hat{e}_r$) and a dipole magnetic field ($\boldsymbol{B}\approx B_r\hat{e}_r+B_\theta\hat{e}_\theta$). The azimuthal component is ignored, since we have assumed that the electron distribution function $f(\boldsymbol{x}, v, \mu, t)$ is gyrotropic. The term on the right-hand side is associated with scattering, and we consider two possible scattering processes that the electrons experience during transport.

2.1.1. Transport Equation in a Radial Magnetic Field

Magnetic focusing depends only on the decrease in the strength of the magnetic field and is independent of its direction. Thus, a radial magnetic field decreasing in strength is the simplest case in practical applications, particularly for open field lines. We are interested in the outward transport of suprathermal electrons in solar flares. For the solar flare background, the magnetic field model proposed by Antiochos et al. (2007) is widely used, which assumes that the radial component is much larger than the other two components, i.e., $B\approx B_r$.

In the case of a radial magnetic field $\boldsymbol{B}\approx B_r\hat{e}_r$, transport Equation (3) reduces to

$$\frac{\partial f}{\partial t}+\mu v\frac{\partial f}{\partial r}-\frac{v(1-\mu^2)}{2}\frac{d\ln B}{dr}\frac{\partial f}{\partial\mu}=\left(\frac{\delta f}{\delta t}\right)_{\rm sc},\tag{4}$$

where r is the radial distance.

Although the magnetic field of a solar flare varies with time, its timescale is much larger than the timescale of suprathermal electrons traveling in the solar corona. For instance, a 10 keV electron with a velocity of roughly 10^4 km s^{-1} needs only 10 s to travel one solar radius, which is much shorter than the timescale of a typical solar flare that is about 1000 s. Hence, it is safe to assume that the magnetic field is approximately "stationary" when suprathermal electrons propagate in the solar corona, which is the condition for the conservation of the magnetic moment. For a detailed radial magnetic field configuration, we first follow the reference scenario provide by the modeling of the solar magnetic field by Banaszkiewicz et al. (1998) and the open magnetic field lines of solar flares by Antiochos et al. (2007). A general form of the outward magnetic field can be expressed as a summation of a series of $B_0/r^{n_{\rm B}}$, where B_0 is the magnetic field at a reference point, and $n_{\rm B}=1, 2, 3, \cdots$. As a magnetic field decreases in strength with radial distance r, the simplest case is $B=B_0/r^2$, which ensures the divergence-free condition of the magnetic field. Hence, the radial derivative of $\ln B$ reduces to $d\ln B/dr=-n_{\rm B}/r$. The specific value of B_0 cancels out, and only the radial variation of the magnetic field (the value of $n_{\rm B}$) remains in transport Equation (4). The electron transport equation in a radial magnetic field has the form of

$$\frac{\partial f}{\partial t}+\mu v\frac{\partial f}{\partial r}+\frac{n_{\rm B}}{2}\frac{v(1-\mu^2)}{r}\frac{\partial f}{\partial\mu}=\left(\frac{\delta f}{\delta t}\right)_{\rm sc}.\tag{5}$$

2.1.2. Transport Equation in a Dipole Magnetic Field

Magnetic focusing depends on the strength of the magnetic field decreasing rather than the direction of the radial evolution of the magnetic field. On the other hand, scattering from Coulomb collisions and wave–particle interactions are accumulative effects and depend on plasma parameters such as density, temperature, and turbulence intensity following the electron transport path along the magnetic field line of flares. As a result, the effects of scattering depend on the spatial structure of the magnetic loops. The prevalent view of the geometry of the coronal magnetic field assumes that it is a magnetic loop whose legs consist of oppositely directed (antiparallel) fields (Benz 2017). A dipole magnetic field is commonly used to model magnetic loops in the solar corona (McClements 1992a) and can be written as

$$B_r=\frac{2M\cos\theta}{r^3},\tag{6}$$

$$B_\theta = \frac{M \sin\theta}{r^3}, \tag{7}$$

where M is a constant, and $r = l \sin^2\theta$, where l is a parameter defining the height from the magnetic field (loop) to the center of the Sun. The magnitude of the dipole field is

$$B = \frac{M}{l^3}\frac{(1 + 3\cos^2\theta)^{1/2}}{\sin^6\theta}. \tag{8}$$

Equations (6)–(8) enable us to calculate the corresponding transport equation from Equation (3) by deriving $\boldsymbol{b}\cdot\nabla f$ and $\boldsymbol{B}\cdot\nabla B/B^2$:

$$\boldsymbol{b}\cdot\nabla f = 4\left(\frac{l-r}{4l-3r}\right)^{1/2}\frac{\partial f}{\partial r} \tag{9}$$

and

$$\frac{\boldsymbol{B}\cdot\nabla B}{B^2} = \frac{3}{r}\left(\frac{l-r}{4l-3r}\right)^{1/2}\left(\frac{8l-5r}{4l-3r}\right). \tag{10}$$

Therefore, the electron transport equation in a dipole field has the form

$$\frac{\partial f}{\partial t} + 4\left(\frac{l-r}{4l-3r}\right)^{1/2} v\mu\frac{\partial f}{\partial r} + \left(\frac{l-r}{4l-3r}\right)^{1/2} \times\left(\frac{8l-5r}{4l-3r}\right)\frac{3}{2}\frac{v(1-\mu^2)}{r}\frac{\partial f}{\partial \mu} = \left(\frac{\delta f}{\delta t}\right)_{\rm sc}. \tag{11}$$

It is easy to see that when $l \gg r$, this transport equation approximates the form of transport Equation (5) with $n_{\rm B} = 3$. Note that r and θ are not independent of each other ($r = l\sin^2\theta$) in the dipole field. We have converted $\partial f/\partial\theta$ to $\partial f/\partial r$ in the process of deriving Equation (11). Therefore, although dipole field transport Equation (11) only has one dimension in configuration space, it is complete in incorporating the effects of both r and θ.

2.1.3. Scattering Terms Associated with Coulomb Collisions and Wave–Particle Interactions

Coulomb collisions and wave–particle interactions with turbulence are two frequently considered scattering mechanisms in the solar corona and winds (McClements 1992b; Reid & Kontar 2013; Effenberger & Petrosian 2018). We introduce the two effects as independent scattering terms ($(\delta f/\delta t)_{\rm sc}$) to the right-hand side of the transport equation and study the role of scattering during the formation of electron beams.

The Coulomb collision operator, describing collisions with a Maxwellian electron background, can be expressed in the plasma rest frame as (Helander & Sigmar 2005)

$$\left(\frac{\delta f}{\delta t}\right)_{\rm cc} = c_\nu\left[\mathrm{erf}\left(\frac{v}{v_{{\rm th}b}}\right) - G\left(\frac{v}{v_{{\rm th}b}}\right)\right]\frac{1}{2v^3}\frac{\partial}{\partial\mu}\left[(1-\mu^2)\frac{\partial f_e}{\partial\mu} + \frac{1}{v^2}\frac{\partial}{\partial v}\left[c_\nu G\left(\frac{v}{v_{{\rm th}b}}\right)v\frac{\partial f_e}{\partial v}\right] + \frac{1}{v^2}\frac{\partial}{\partial v} \times\left[\frac{2c_\nu}{v_{{\rm th}b}^2}v^2 G\left(\frac{v}{v_{{\rm th}b}}\right)f_e\right], \tag{12}$$

where $v_{{\rm th}b}$ is the thermal velocity of the background Maxwellian electrons, $k_{\rm B}$ is the Boltzmann constant, G is the Chandrasekhar function, erf is the error function, and

$$c_\nu = \frac{4\pi n_j e^4 \ln\Lambda}{m_e^2}. \tag{13}$$

Equation (12) is consistent with the e–e collision part of the collision operator used in Smith et al. (2012). Though the collision rates for e–e and e–p Coulomb collisions are comparable (pitch angle scattering), the energy change to electrons experiencing e–p collisions (velocity diffusion) is very small, about m_e/m_i times smaller than the e–e collisions due to the conservation of momentum. Therefore, we consider only Coulomb collisions with background electrons, which is what Jeffrey et al. (2019) assumed as well.

Turbulent scattering is another significant effect (Reid et al. 2011), but our knowledge of solar corona turbulence is poor, and its origin and intensity are uncertain. In this paper, we choose the most widely accepted wave–particle interaction scattering terms associated with whistler turbulence given in Schlickeiser (1989):

$$\left(\frac{\delta f}{\delta t}\right)_{\rm wp} = \frac{\partial}{\partial\mu}\left(D_{\mu\mu}\frac{\partial f}{\partial\mu}\right) + \frac{1}{v^2}\frac{\partial}{\partial v}\left(\frac{v^2}{m^2}D_{vv}\frac{\partial f}{\partial v}\right) + \frac{\partial}{\partial\mu}\left(\frac{1}{m}D_{\mu v}\frac{\partial f}{\partial v}\right) + \frac{1}{v^2}\frac{\partial}{\partial v}\left(\frac{v^2}{m}D_{v\mu}\frac{\partial f}{\partial\mu}\right). \tag{14}$$

This is a quasi-linear model of wave–particle scattering. The corresponding diffusion tensor for nonrelativistic electrons is expressed as (Steinacker & Miller 1992; Tang et al. 2022)

$$D_{vv} = \frac{\Omega_{\rm e} m^2 c^2 \pi}{3}\frac{\rm A}{\rm a}\left(\frac{\beta|\mu|}{\rm a}\right)^{\frac{s-1}{3}}(1-\mu^2), \tag{15a}$$

$$D_{\mu v} = D_{v\mu} = -\frac{\Omega_{\rm e} mc\pi}{3}\frac{\rm A}{\rm a}\left[\frac{\mu}{|\mu|}\left(\frac{\beta|\mu|}{\rm a}\right)^{\frac{s-2}{3}} + \frac{\mu}{\beta}\left(\frac{\beta|\mu|}{\rm a}\right)^{\frac{s-1}{3}}\right](1-\mu^2), \tag{15b}$$

$$D_{\mu\mu} = \frac{\Omega_{\rm e}\pi}{3}\frac{\rm A}{\rm a}\left[\left(\frac{\beta|\mu|}{\rm a}\right)^{\frac{s-3}{3}} + \frac{2\mu}{\beta}\frac{\mu}{|\mu|}\left(\frac{\beta|\mu|}{\rm a}\right)^{\frac{s-2}{3}} + \left(\frac{\mu}{\beta}\right)^2\left(\frac{\beta|\mu|}{\rm a}\right)^{\frac{s-1}{3}}\right](1-\mu^2), \tag{15c}$$

where $\beta = v/c$, $a = \Omega_{\rm e}^2/\omega_{\rm pe}^2$, $s = 2$ is the spectral index of whistler waves, and A is an artificial normalization constant related to the magnitude of the energy spectral densities of the turbulence. In the corona, the turbulence mean free path is much larger than the Coulomb mean free path and becomes comparable to or less than the Coulomb mean free path above a few tens of solar radii (Pierrard et al. 2011). Therefore, the effect of turbulence adversely affecting the formation of electron beams should be less important than that of Coulomb collisions in the corona.

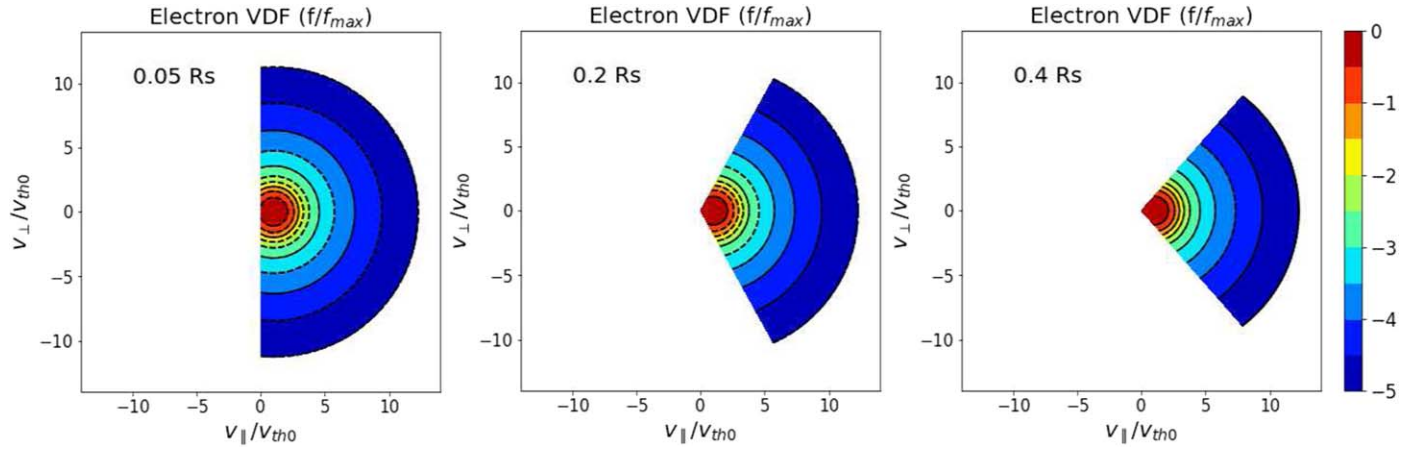

Figure 2. The 2D contour plots of the normalized electron VDF ($f/f_{\max}$) in the moving frame at 0.05, 0.2, and 0.4 R_s in the case of $\delta = 0.8$, $\alpha = 4$, $U_d = 1v_{th0}$, and $B = B_0/r^2$. The influence of magnetic focusing on the radial evolution of the electron VDF is obvious. The maximum pitch angle of the electron VDF decreases, while the parallel part does not change.

2.2. Coronal Background

Coulomb collisional and turbulence scattering depend on the background plasma properties in the corona. We assume that the temperature and number density profiles of the Maxwellian background of electrons and protons are prescribed. The mass conservation of solar wind expansion results in a strong radial gradient in plasma density, decreasing with radial distance as r^{-2} and even faster in the solar wind acceleration region. We choose the empirical radial profile of background electron number density reported by Baumback (1937) and Lemaire & Stegen (2016):

$$n_b(r) = 10^8\left[2.99\left(\frac{r}{R_s}\right)^{-16} + 1.55\left(\frac{r}{R_s}\right)^{-6} + 0.036\left(\frac{r}{R_s}\right)^{-1.5}\right]\mathrm{cm}^{-3}. \quad (16)$$

For simplicity, we assume that the temperature of the Maxwellian background of electrons varies as a power law:

$$T_b(r) = 1 \times 10^7\left(\frac{r}{R_s}\right)^{-0.64}\mathrm{K}. \quad (17)$$

The suprathermal electron velocity distribution function (VDF) produced at the acceleration region by MR is injected at an inner boundary r_0. It is well known that solar flares accelerate electrons to a power-law energy distribution (Krucker et al. 2009; Lin 2011; Zharkova et al. 2011) in the MR region. Theoretical studies and particle-in-cell simulations show that power-law energetic electrons can be produced in the diffusion region of MR (Zank et al. 2014; Che & Zank 2020; Che et al. 2021). For simplicity and generality, in our calculation, we assume that these suprathermal electrons have an isotropic velocity distribution function in a moving frame with a velocity U_d far below the threshold to trigger ETSI. Suprathermal electrons with such a least confined distribution in velocity space would be the least likely to evolve into electron beams. Therefore, a combination of a Maxwellian (f_m) and a power law (f_p) is chosen to mimic the initial suprathermal energetic electron VDF with a bulk motion velocity U_d, and

$$U_d \leqslant v_{th}.$$

Initially, U_d is not large enough to trigger ETSI at the acceleration region,

$$f(v, \mu \geqslant 0) = \delta f_m(v, \mu) + (1 - \delta) f_p(v, \mu), \quad (18)$$

$$f_m(v, \mu) = n_0\left(\frac{m}{2\pi k_B T_{c0}}\right)^{3/2} \times \exp\left\{-\frac{m}{2k_B T_{c0}}[(v\mu - U_d)^2 + v^2(1 - \mu^2)]\right\}, \quad (19)$$

$$f_p(v, \mu) = n_0\frac{1}{4\pi}\frac{\alpha - 3}{v_c^{3-\alpha}} \times \{[(v\mu - U_d)^2 + v^2(1 - \mu^2)]^{1/2}\}^{-\alpha}, \quad (v\mu - U_d)^2 + v^2(1 - \mu^2) \geqslant v_c^2, \quad (20)$$

where δ is the weight of the Maxwellian component f_m, T_{c0} is the temperature of the Maxwellian component, n_0 is the total electron number density at the inner boundary r_0, v_c is the critical velocity separating the power-law component (suprathermal electrons) from the Maxwellian, and α is the spectral index of the power-law component. The first graph in Figure 2 shows an example of the electron VDF at the inner boundary in the ($v_\parallel$, $v_\perp$) plane in the case of $\delta = 0.8$, $\alpha = 4$, $U_d = 1v_{th0}$, $n_B = 2$, and $(\delta f/\delta t)_{sc} = 0$.

We solve transport Equation (5) numerically with the boundary conditions (Equations (18)–(20)) to study the transport of suprathermal electrons in the corona. Assuming the accelerated electrons are injected in the MR acceleration region in the lower corona (Reid et al. 2011; Chen et al. 2013; Cairns et al. 2018), the inner boundary is chosen as $r_0 = 0.05$ R_s above the surface of the Sun, where R_s is the solar radius. The outer boundary of $\sim$2.05 R_s is the typical size of the magnetic loops (Antiochos et al. 2007). We choose a critical velocity $v_c = 1.5v_{th0}$, where $v_{th0} = (2k_B T_{c0}/m)^{1/2}$ is the target/test electron thermal velocity at the inner boundary (the acceleration region). We adjust the parameters α and U_d to mimic the diverse power-law electron energy spectra and the bulk motion of electron outflows produced by MR acceleration.

Table 1
Combinations of Different Parameters

Label	Magnetic Configuration	α	$U_d(v_{th0})$	Scattering
G1	$B = B_0/r^2$	4	0	No scattering
G2	$B = B_0/r^3$	4	0	No scattering
G3	$B = B_0/r$	4	1	No scattering
G4	$B = B_0/r^2$	4	1	No scattering
G5	$B = B_0/r^3$	4	1	No scattering
G6	$B = B_0/r^4$	4	1	No scattering
G7	$B = B_0/r^3$	4	0.5	No scattering
G8	$B = B_0/r^3$	8	0.5	No scattering
G9	$B = B_0/r^3$	6	0.5	No scattering

We mimic the magnetic field line of flares with a variety of curvatures by adjusting the value of n_B. The combinations of various α, U_d, and n_B used in the calculation and their labels are listed in Table 1. The stationary numerical solution is obtained after the code approaches the steady final state.

3. Numerical Results

3.1. Transport of Electrons in Radial Magnetic Field without Scattering

Magnetic focusing is a direct consequence of the conservation of the magnetic moment defined as $\mu_M = mv_\perp^2/2B$. It plays an essential role in the formation of electron beams when suprathermal electrons propagate upward along a decreasing magnetic field. Magnetic focusing is independent of the transport path of electrons and only depends on the strength of the magnetic field, while Coulomb collisional and turbulent scattering depends on the transport path of the electrons. Thus, the shortest transport path for electrons is along the radial direction, which is the simplest case, and it is important to study the transport of suprathermal electrons in a radial magnetic field without any scattering mechanisms, i.e., $(\delta f/\delta t)_{sc} = 0$ in transport Equation (5). Thereafter, we introduce Coulomb collisional and turbulence scattering and examine the transport of suprathermal electrons in radial and dipole magnetic fields, respectively.

First, we consider a case in which the scattering term on the right-hand side of transport Equation (5) is ignored, i.e., $(\delta f/\delta t)_{sc} = 0$. In such a case, we can obtain an analytic solution with a given boundary condition by the method of characteristics (Sone & Sugimoto 1993; Tang et al. 2020),

$$f(r, v, \mu) = \begin{cases} f_0(r_0, v, \mu), & \left[1 - \left(\frac{r_0}{r}\right)^{n_B}\right]^{1/2} < \mu < 1 \\ 0. & -1 < \mu < \left[1 - \left(\frac{r_0}{r}\right)^{n_B}\right]^{1/2}, \end{cases} \tag{21}$$

where $f_0(r_0, v, \mu)$ is any given inner boundary condition at r_0. The radial evolution of the analytic solution (Equation (21)) is shown in Figure 2, where the inner boundary is $r_0 = 0.05\ R_s$ above the surface of the Sun. The electron VDF $f_0(r_0, v, \mu)$ at the inner boundary is a combination of a drifting Maxwellian and a power law, i.e., $\delta = 0.8$, $\alpha = 4$, and $U_d = 1v_{th0}$, and the background magnetic field is radial, i.e., $n_B = 2$. The influence of magnetic focusing on the radial evolution of the electron VDF is apparent. As the distance increases, the maximum pitch angle of the electron VDF decreases due to the focusing induced by a decreasing magnetic field, and the electron VDFs become increasingly anisotropic with increasing distance. The maximum value of the electron parallel velocity increases while that of the perpendicular velocity decreases, leading to the formation of a group of fast outward-moving electrons—an electron beam.

The electron beam velocity is the essential parameter determining the triggering of ETSI (Che 2016). The electron beam velocity is defined as

$$u_b = \frac{\int_{v_{min}(r,\mu)}^{\infty}\int_{\mu_{min}(r)}^{1} vf d\boldsymbol{v}}{\int_{v_{min}(r,\mu)}^{\infty}\int_{\mu_{min}(r)}^{1} f d\boldsymbol{v}}, \tag{22}$$

where $\mu_{min}(r) = [1 - (r_0/r)^{n_B}]^{1/2}$ is the cosine of the maximum pitch angle of the electron VDF at a distance r, which is given by the analytic solution (Equation (21)). Here $v_{min}(r, \mu) = U_d\mu + [U_d^2(\mu^2 - 1) + v_c^2]^{1/2}$ is the critical velocity of the power-law component. This definition is similar to the definition of the mean electron velocity within the beam (Reid & Kontar 2018b). In the case of $U_d \neq 0$, $f(r, v, \mu)$ and v_{min} are highly anisotropic, and the analytical solution of u_b is hard to obtain.

The numerical radial evolution of the electron beam velocity u_b in the rest frame of the Sun is shown in Figure 3 for different coronal backgrounds. The label numbers of the curves indicate the simulation runs, and their parameters (α, U_d, and n_B) are listed in Table 1. It can be seen that under all conditions, u_b increases sharply from the inner boundary 0.05 to 0.4 R_s (i.e., over a distance of $\sim$0.4 R_s) and approaches a saturated value at the outer boundary. The left panel has a Maxwellian velocity distribution with weight $\delta = 1$ at the inner boundary, and the right panel is a Maxwellian with weight $\delta = 0.8$ plus a power-law velocity tail with index $\alpha = 4$ and weight 0.2 ($=1 - \delta$). The index $\alpha = 4$ is estimated according to the lower bound of the observable index of electron energy spectra, which is about 3 (Lin et al. 1973, 1981; Krucker et al. 2007; Benz 2017), and the weight 0.2 is estimated by the typical acceleration efficiency found in particle-in-cell simulations (Che & Zank 2020; Che et al. 2021). Different velocity starting points for u_b are caused by the different drifting velocities U_d ($0v_{th0}$, $0.5v_{th0}$, and $1v_{th0}$) of the initial electron VDF at the inner boundary.

Figure 3 shows that for electrons of a Maxwellian VDF (left panel; $\delta = 1$) transporting upward from the acceleration region, magnetic focusing can rapidly increase the bulk velocity of suprathermal electrons to nearly twice that of the thermal velocity of the local background coronal plasma over a distance of about 0.4 R_s. As a comparison, for an electron VDF possessing a suprathermal portion, i.e., a combination of Maxwellian and power-law spectrum tail (right panel; $\delta = 0.8$), magnetic focusing can increase the bulk velocity of suprathermal electrons to an even higher speed over the same distance of 0.4 R_s, as much as three to five times the electron thermal velocity in the acceleration region v_{th0}. In the environment of the solar corona, the decrease in electron temperature with distance leads to a decrease in the electron thermal velocity ($v_{th} < v_{th0}$). Therefore, in the corona, the electron beam velocity u_b can likely be increased to a much larger value than the local

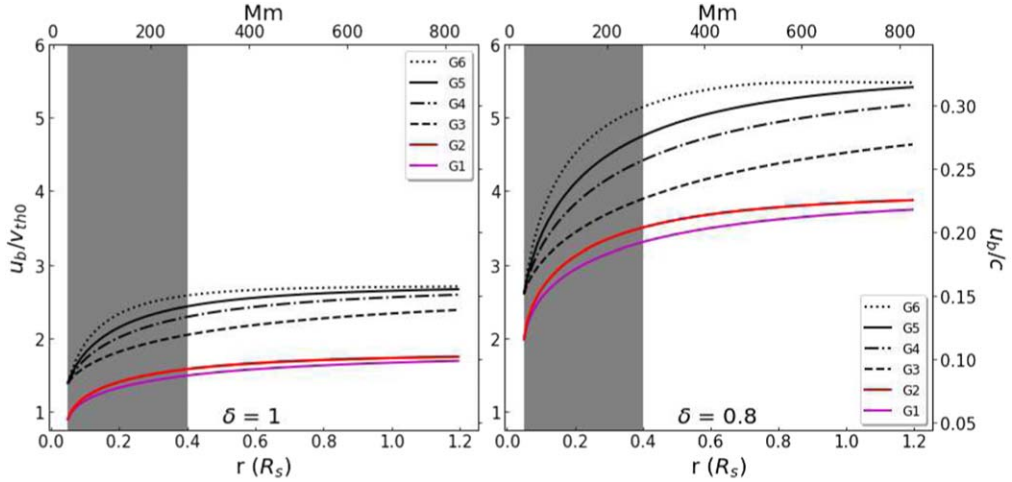

Figure 3. Radial evolution of the velocity of suprathermal electrons u_b without scattering terms, normalized by v_{th0} and c in the rest frame of the Sun using a electron temperature $T_{c0} = 10^7$ K and $v_{th0} = (2k_B T_{c0}/m)^{1/2}$ of the acceleration region. In the left panel, the electron VDF at the inner boundary is a Maxwellian only ($\delta = 1$). In the right panel, the electron VDF at the inner boundary is a combination of a Maxwellian with weight $\delta = 0.8$ and an isotropic power law with $\alpha = 4$ and weight 0.2 ($=1 - \delta$). The shaded areas indicate the distance range from 0.05 to 0.4 R_s. The labels of the curves (G1–G6) represent the simulation runs and their parameters (α, U_d, and n_B), which are listed in Table 1.

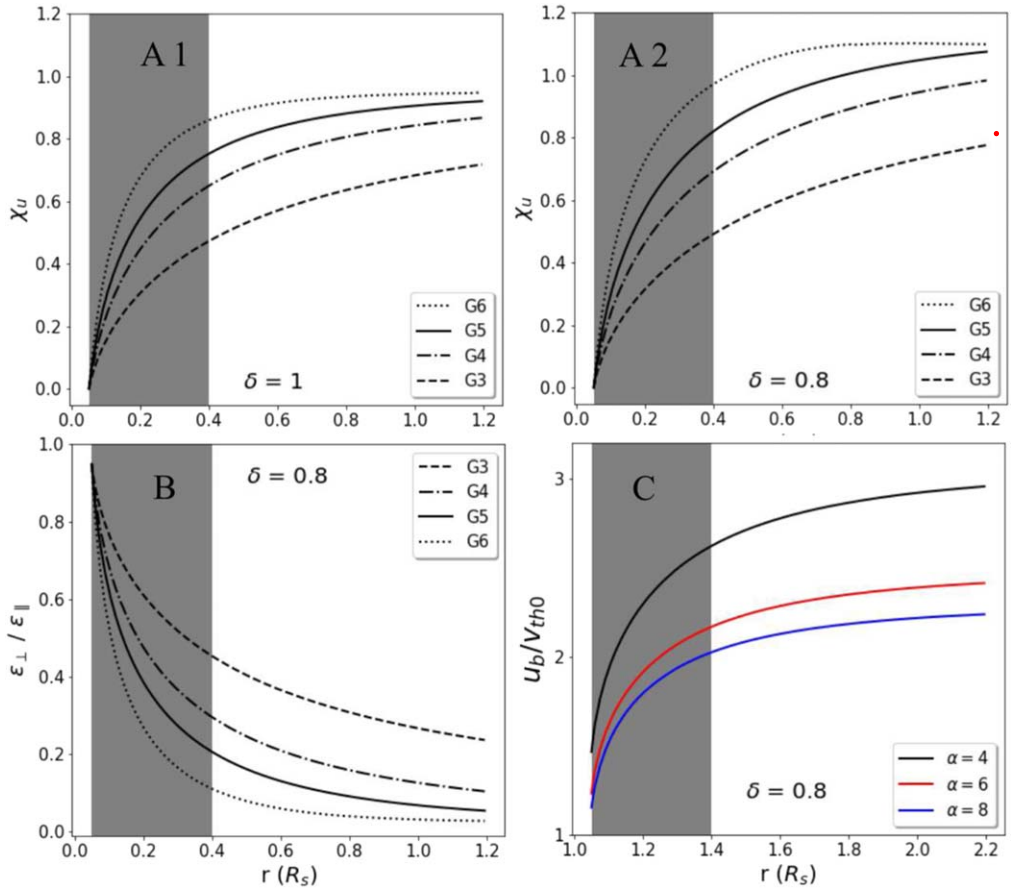

Figure 4. Panels (A1) and (A2): radial evolution of the percentage increase in the beam velocity of suprathermal electrons χ_u. Panel (A1) corresponds to a Maxwellian velocity distribution (left panel of Figure 3), and panel (A2) corresponds to a Maxwellian with weight $\delta = 0.8$ plus a power-law velocity tail (right panel of Figure 3). Panel (B): radial evolution of $\epsilon_\perp/\epsilon_\parallel$ for suprathermal electrons. Line colors and styles have the same meaning as in Figure 3. Panel (C): radial revolution of u_b with different power-law indices $\alpha = 4$, 6, and 8. The shaded areas indicate the distance range from 0.05 to 0.4 R_s. The labels of the curve represent the simulation runs and their parameters (α, U_d, and n_B), which are listed in Table 1.

electron thermal velocity v_{th}, i.e., $u_b \gg v_{th}$. These fast electron beams can trigger a strong ETSI and produce coronal type III radio bursts (Che 2016; Che et al. 2017), which is consistent with observations that find that coronal type III radio bursts are always above a certain distance from the acceleration region (Chen et al. 2013, 2018).

To illustrate how the rate of radial variation of the magnetic field (n_B) affects the radial evolution of the electron beam

velocity, we define the percentage increase of the electron beam velocity as $\chi_u = (u_b - u_{b0})/u_{b0}$, where u_{b0} is the initial u_b at the inner boundary. The radial evolution of the percentage increases χ_u are shown in panels (A1) and (A2) in Figure 4. Like Figure 3, panel (A1) is a Maxwellian VDF with weight $\delta = 1$ at the inner boundary, and panel (A2) is a Maxwellian with weight $\delta = 0.8$ plus a power-law velocity tail with index $\alpha = 4$ and weight 0.2. The percentage increases χ_u in panel (A2) are larger than those in panel (A1), indicating that the effect of magnetic focusing on electrons with a power-law tail leads to a higher bulk velocity than the case of Maxwellian distribution only. Therefore, magnetic focusing can increase the electron bulk velocity much more rapidly if more suprathermal energetic electrons with a power-law tail are present, thus triggering ETSI and producing coronal type III radio bursts. Moreover, the n_B in the magnetic field $B = B_0/r^{n_B}$ also affects the radial evolution of u_b and the corresponding percentage increase χ_u. From curve G3 to G6, n_B increases from 1 to 5 (see Table 1). As n_B increases, both the electron beam velocity u_b (see Figure 3) and the percentage increase χ_u (see Figure 4) increase faster and reach a larger value. Consequently, in a more rapidly decreasing magnetic field, we expect more coronal type III radio bursts to occur at distances closer to the acceleration region of MR.

Magnetic focusing increases the bulk velocity of electrons along the magnetic field line of flares by transferring electron kinetic energy from the perpendicular to the parallel direction. We define and calculate the ratio of the perpendicular to the parallel kinetic energy of electrons ($\epsilon_\perp/\epsilon_\parallel$) as

$$\frac{\epsilon_\perp}{\epsilon_\parallel} = \frac{\int \frac{1}{2} m v_\perp^2 f d\boldsymbol{v}}{\int \frac{1}{2} m v_\parallel^2 f d\boldsymbol{v}}. \quad (23)$$

The radial evolution of the electron kinetic energy ratio $\epsilon_\perp/\epsilon_\parallel$ is shown in panel (B) of Figure 4 in the case of $\delta = 0.8$, and $U_d = v_{th0}$, i.e., the case of panel (A2). For an isotropic electron VDF at the inner boundary, the kinetic energy ratio is 2, since an isotropic VDF has 1 degree of freedom in the parallel direction and 2 degrees of freedom in the perpendicular direction. However, in our case, the electron VDF with a bulk motion velocity $U_d \neq 0$ is anisotropic; hence, the electron kinetic energy ratio is less than 2. Furthermore, the radial evolution of the kinetic energy ratio decreases with distance, which contrasts with the radial evolution of the electron bulk velocity u_b and χ_u. It is noticeable that the kinetic energy ratio drops sharply in the distance range from 0.05 to 0.4 R_s, while u_b and χ_u, on the contrary, increase sharply in the same distance range. Moreover, the radial evolution of the kinetic energy ratio caused by magnetic focusing is dominated by the magnitude of n_B; the larger the n_B (curves G5 and G6), the faster the decrease of the kinetic energy ratio.

Panel (C) in Figure 4 shows the radial evolution of the velocity of suprathermal electrons u_b with different energy spectral indices α. The electron bulk speed u_b with a smaller spectral index α has a higher initial value, since the electron VDF with a smaller spectral index α possesses more suprathermal electrons. The smaller spectral index α leads to a faster increase of u_b with radial distance. Similarly, the maximum increase is in the same gray shaded area.

Table 2
Combinations of Different Parameters

Label	Magnetic Configuration	α	$U_d(v_{th0})$	Scattering
G10	Radial $B = B_0/r^3$	4	0	No scattering
G11	Radial $B = B_0/r^3$	4	0	Coulomb collision
G12	Dipole $l = 9\ R_s$	4	0	Coulomb collision
G13	Dipole $l = 5\ R_s$	4	0	Coulomb collision
G14	Dipole $l = 3\ R_s$	4	0	Coulomb collision
G15	Radial $B = B_0/r^3$	4	0	Whistler turbulence
G16	Radial $B = B_0/r^3$	4	0	Collision and turbulence

3.2. Transport of Electrons in Radial and Dipole Magnetic Fields with Coulomb Collisional and Turbulent Scattering

Coulomb collisions are associated with the particle number density, and the turbulent scattering depends on the strength of the local turbulence. As a result, suprathermal electrons experience different scattering strengths while being transported on different forms of magnetic loops. We choose radial and dipole magnetic fields as two examples to investigate how the spatial shape of magnetic field loops affects the formation of electron beams.

With the discussion of the transport equation in a dipole magnetic field in Equation (11), the transport equation of the dipole field reduces to the form of the radial magnetic field transport equation with $n_B = 3$ when the dipole height parameter $l \gg r$. Accordingly, we choose radial transport Equation (5) with $n_B = 3$ as the primary case for comparison. On the other hand, our calculations show that the saturation of the growth of the suprathermal electron bulk velocity requires a minimum heliocentric distance of 3 R_s, so we choose the lower limit of l as $l = 3\ R_s$. Our calculations show that the results for the dipole field with $l = 5\ R_s$ are similar to that found with radial magnetic fields. Thus, we choose $l = 3$, 5, and 9 R_s to demonstrate the impact of the shape of magnetic loops. The combinations of different magnetic configurations, plasma parameters, and scattering effects are listed in Table 2.

In Figure 5, we show the radial evolution of the electron beam velocity u_b for the cases of scattering in both radial and dipole fields, as listed in Table 2. The case of a radial magnetic field with $n_B = 3$ (i.e., curve G2 in Figure 3) used as a reference for the study of the effect of scattering and dipole fields is denoted as G10. In the following discussions, by comparing G10 with the rest of the curves, we investigate the competition between magnetic focusing, Coulomb collisional scattering, and turbulent scattering during the transport of suprathermal electrons and the formation of coronal electron beams.

Curve G11 (blue) is the result of Coulomb collisional scattering in a radial magnetic field. Comparing G11 with G10, the introduction of the Coulomb collisional scattering causes u_b to increase more slowly and saturate at a lower speed. However, u_b still rises sharply over 300 Mm (shaded area), and its saturated speed reaches about triple the electron thermal velocity of the acceleration region ($\approx 3v_{th0}$).

The effect of Coulomb collisions on electrons is cumulative and depends on the electron propagation path along the magnetic field line of flares. The electron transport path in a dipole magnetic field is longer than in a radial magnetic field. Hence, electrons experience a longer Coulomb collisional scattering time in a dipole magnetic field than in a radial

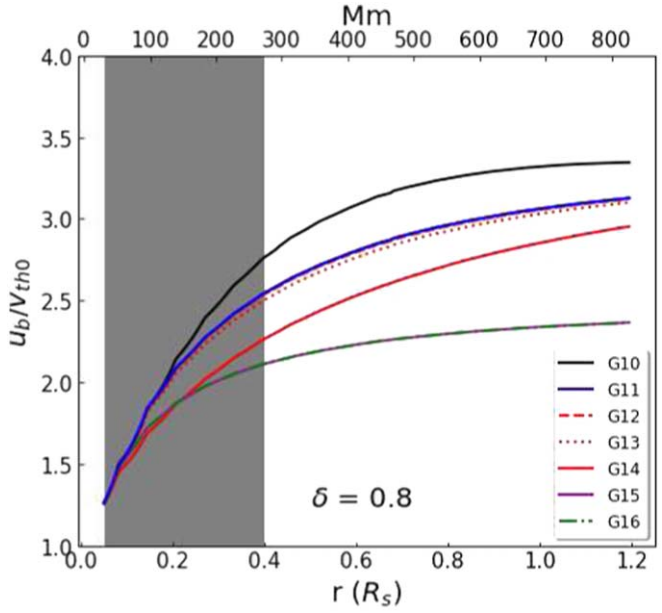

Figure 5. Radial evolution of the bulk velocity of suprathermal electrons u_b with scattering, normalized by v_{th0} and c in the rest frame of the Sun using a temperature $T_{c0} = 10^7$ K. The shaded areas indicate the distance range from 0.05 to 0.4 R_s. The labels of the curves (G10–G16) denote the simulation runs and their parameters (magnetic configurations, plasma parameters, and scatterings), which are listed in Table 2.

magnetic field. The competition between magnetic focusing and Coulomb collisional scattering in three dipole magnetic fields with different sizes is shown by G12 (red dashed curve; $l = 9\ R_s$), G13 (red dotted curve; $l = 5\ R_s$), and G14 (red solid curve; $l = 3\ R_s$). We note that G12 overlaps G11, and G13 is very close to G11, implying that transport Equation (11) in the dipole magnetic field can be approximated by the form with a radial magnetic field of $n_B = 3$ when $l > 5\ R_s$. The slowest increase in u_b and the lowest saturated speed of u_b are shown in G14, which is the result of Coulomb collisional scattering in the dipole magnetic field with the lower limit $l = 3\ R_s$. In this case, electrons travel the longest path along the magnetic field line and experience the strongest Coulomb collisional scattering. However, we still find that the saturated u_b can reach about triple the electron thermal velocity of the acceleration region ($\approx 3v_{th0}$), and magnetic focusing dominates Coulomb collisions leading to the formation of coronal electron beams.

Turbulent scattering depends on the strength of the turbulence, which is uncertain due to the paucity of observations. Thus, we instead consider an estimate for the upper limit for turbulent scattering. We choose much stronger whistler turbulence than the observations expect (a large value of A in Equation (15a)) in a radial magnetic field, and curve G15 (magenta) shows the result. This choice leads to the slowest increase and lowest saturated speed for u_b. The saturated speed of u_b of G15 is still more than twice the electron thermal velocity of the acceleration region ($>2v_{th0}$). The intensity of turbulence in the solar corona is uncertain, but it is commonly expected to be less important than Coulomb collisions. Our numerical result does not imply that whistler turbulence is stronger than Coulomb collisions in the solar corona but rather gives an upper limit estimate of the effect of turbulent scattering on the radial evolution of u_b. We then add Coulomb collisional scattering into G15, which represents a combination of turbulent scattering and magnetic focusing in a radial field, and the result is shown by G16 (green dashed curve). We note that G16 overlaps G15, indicating that both the Coulomb collisional and turbulent scattering do not change the role and importance of magnetic focusing in electron beam formation. It is noteworthy that, although the specified strong turbulence scattering produces the most significant decrease in u_b, the final saturated speeds of u_b of G15 and G16 are still more than twice the electron thermal velocity of the acceleration region ($>2v_{th0}$).

In conclusion, Coulomb collisional and turbulent scattering slightly change the radial evolution of the electron beam velocity u_b in the solar corona, as shown in Figure 5. The beam speed u_b increases sharply over a distance of 0.4 R_s (shaded area), and the saturated speed of u_b reaches more than twice or triple the electron thermal velocity of the acceleration region ($>2v_{th0}$ or $3v_{th0}$). If it is considered that the local coronal temperature is much lower than that in the acceleration region, theoretically, u_b is much larger than the threshold of EKHI and can trigger coronal type III radio bursts within the observational distances. Magnetic focusing overrides Coulomb collisional and turbulent scattering and drives the formation of electron beams in the solar corona. In next section (Section 4), we will use the observational data to further demonstrate this point.

4. Conclusions and Applications

Coronal type III radio bursts are signatures of electron beams propagating in the solar corona. Observations of coronal type III radio bursts indicate that the coronal electron beams are commonly and frequently produced within the solar corona. In this paper, by numerically solving the kinetic transport equation, we investigate the transport of suprathermal energetic electrons and the formation of coronal electron beams. Three competing effects that impact the formation of electron beams are considered: magnetic focusing, Coulomb collisions, and turbulence. Compared to Coulomb collisions and turbulence that can affect the formation of electron beams through scattering, magnetic focusing is intrinsic and the only effect to continuously form electron beams. Unlike previous studies (Li et al. 2006; Reid et al. 2011), we consider the formation of high bulk velocity coronal electron beams before producing type III radio bursts. We do not address the generation of Langmuir waves and the maintenance of electron beams in interplanetary space after they trigger type III radio bursts in the solar corona.

Our numerical results show that although Coulomb collisions and turbulent scattering attempt to prevent the formation of electron beams, their effects are much weaker than that of magnetic focusing. Magnetic focusing significantly suppresses the effects of scattering, which results in the formation of coronal electron beams in the solar corona. Electron beams develop efficiently within the observationally desired distance of ~300 Mm above the photosphere. The bulk velocity of electron beams reaches a saturated speed as high as 0.1c–0.3c, which satisfies the ETSI threshold for coronal type III radio bursts. In the case of suprathermal energetic electrons with a harder power-law energy spectrum, the electron beams achieve a higher velocity, implying that the locations of coronal type III radio bursts depend on the energetic electron spectral index. Consequently, suprathermal energetic electrons with a harder spectrum may be able to trigger the ETSI at a location closer to the acceleration region. The specific spatial shape of the

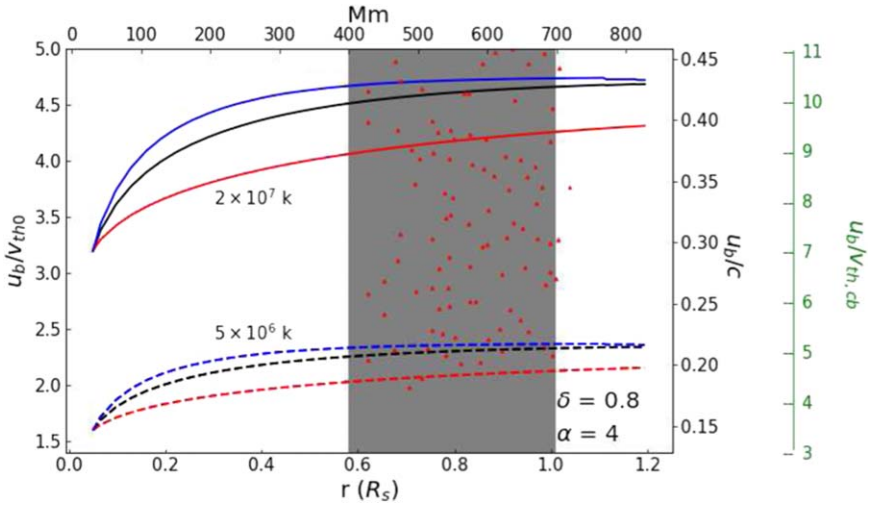

Figure 6. Electron beam velocities (red dots) as a function of distance from the Sun for coronal type III bursts given by Reid & Kontar (2018a). Blue, black, and red solid/dotted lines represent the magnetic field decrease as r^{-5}, r^{-3}, and r^{-1}. The temperatures of the coronal background and acceleration region are 10^6 and 10^7 K, respectively. Calculated bulk velocities are normalized by the electron thermal velocity of the acceleration region (u_b/v_{th0}; left black y-axis) and coronal background ($u_b/v_{the,cb}$; right green y-axis). The shaded area indicates the distance beyond 0.6 R_s (400–700 Mm) where coronal type III radio bursts are frequently observed.

magnetic field (radial or dipole magnetic field) has little effect on the formation of electron beams, since the dipole magnetic field produces the same result as the radial field when the height parameter of the dipole field $l \geqslant 5\ R_s$.

The impact of Coulomb collisions and turbulence scattering on the formation of electron beams in the solar corona is negligible compared with magnetic focusing. The electron Coulomb collision rate in the inner corona is $\nu_e \sim 10^{-6} n_e T_e \sim 10^{-4}$ s^{-1}, and the Coulomb heating timescale is about 10^4 s. Our numerical model shows that it takes less than 200 s in real time for the entire system to reach a steady state. In such a short time, neither Coulomb collisions nor turbulent scattering can efficiently affect the formation of an electron beam.

By comparing with observed electron beam velocities, we can estimate the coronal plasma environment of coronal type III radio bursts. In Figure 6, red dots show the radial distribution of observed electron beam velocities for coronal type III bursts given by Reid & Kontar (2018a). Theoretically, the electron beam velocities are calculated using two different initial temperatures T_{c0} (2×10^7 and 5×10^6 K) in the acceleration region. The radial evolution of electron beam velocities normalized by the electron thermal velocity in the acceleration region (u_b/v_{th0}; left black y-axis) and the coronal background ($u_b/v_{the,cb}$; right green y-axis) is plotted. Coronal type III radio bursts are observed at a distance beyond 0.6 R_s (shaded area; 400–700 Mm), which is above the region where the electron beam velocity increases sharply (from 0.05 to 0.4 R_s, indicated by the shaded areas in Figures 3 and 5). The electron beam velocities do not increase much thereafter and tend to plateau in this region. In considering the range of the observed (red dots) beam speeds and noting that the theoretical beam speeds bracket this range, Figure 6 suggests that the temperature in the acceleration region ranges from 5×10^6–2×10^7 K, which is consistent with observations. A noticeable phenomenon is that the bulk velocities of some coronal electron beams can reach 10 times the background electron thermal velocity (Krucker et al. 2007; Reid et al. 2011; Benz 2012, 2017; Chen et al. 2013, 2018), which is much larger than the threshold of the ETSI. Figure 6 suggests that the velocity of electron beams in general is three times larger than the background electron thermal velocity at $T_{the,cb} = 10^6$ K, but some can reach $10v_{the,cb}$ (right green y-axis). From the observations and our model, we can infer that the acceleration region and background plasma have a distinct boundary where the temperature has a sharp decrease. This can explain why some beam velocities can reach speeds up to $10v_{the,cb}$, which is much larger than the theoretical threshold to trigger ETSI ($3v_{th0}$). Such a high-velocity electron beam can trigger a strong ETSI, generating long-lived coronal type III radio bursts, which is consistent with theory (Che et al. 2017) and observations (Reid et al. 2011).

We mention that magnetic focusing also impacts the development of downward-moving electron beams (return currents; Effenberger & Petrosian 2018). However, the plasma environment for downward-moving beams is more complex than that for upward beams (Benz 2017), requiring further study.

Acknowledgments

B.T. and H.C. acknowledge partial support by NASA HSR program No. 80NSSC21K0031, Heliophysics Career award No. 80NSSC19K1106, and NSF CAREER 2144324. The authors acknowledge the partial support of NSF EPSCoR RII-Track-1 cooperative agreement OIA-2148653.

ORCID iDs

Bofeng Tang https://orcid.org/0000-0002-2261-6629
Haihong Che https://orcid.org/0000-0002-2240-6728
Gary P. Zank https://orcid.org/0000-0002-4642-6192

References

Antiochos, S., DeVore, C., Karpen, J., & Mikić, Z. 2007, ApJ, 671, 936
Aschwanden, M. J., & Parnell, C. E. 2002, ApJ, 572, 1048
Banaszkiewicz, M., Axford, W., & McKenzie, J. 1998, A&A, 337, 940
Baumback, S. 1937, AN, 263, 121
Benz, A. O. 2012, Plasma Astrophysics: Kinetic Processes in Solar and Stellar Coronae, Vol. 184 (Berlin: Springer)
Benz, A. O. 2017, LRSP, 14, 2
Beresnyak, A. 2016, ApJ, 834, 47

Cairns, I. H., Lobzin, V., Donea, A., et al. 2018, NatSR, 8, 1676
Che, H. 2016, MPLA, 31, 1630018
Che, H., & Goldstein, M. 2014, ApJL, 795, L38
Che, H., Goldstein, M., Salem, C., & Viñas, A. 2019, ApJ, 883, 151
Che, H., Goldstein, M. L., Diamond, P. H., & Sagdeev, R. Z. 2017, PNAS, 114, 1502
Che, H., & Zank, G. 2020, ApJ, 889, 11
Che, H., Zank, G., Benz, A., Tang, B., & Crawford, C. 2021, ApJ, 908, 72
Chen, B., Bastian, T. S., White, S. M., et al. 2013, ApJL, 763, L21
Chen, B., Yu, S., Battaglia, M., et al. 2018, ApJ, 866, 62
Desai, M., Mitchell, D., McComas, D., et al. 2022, ApJ, 927, 62
Effenberger, F., & Petrosian, V. 2018, ApJL, 868, L28
Ergun, R., Larson, D., Lin, R., et al. 1998, ApJ, 503, 435
Eyink, G., Vishniac, E., Lalescu, C., et al. 2013, Natur, 497, 466
Ginzburg, V., & Zhelezniakov, V. 1958, SvA, 2, 653
Helander, P., & Sigmar, D. J. 2005, Collisional Transport in Magnetized Plasmas, 4 (Cambridge: Cambridge Univ. Press)
Jeffrey, N. L., Kontar, E. P., & Fletcher, L. 2019, ApJ, 880, 136
Kowal, G., Falceta-Gonçalves, D. A., Lazarian, A., & Vishniac, E. T. 2017, ApJ, 838, 91
Krucker, S., Kontar, E., Christe, S., & Lin, R. 2007, ApJL, 663, L109
Krucker, S., Oakley, P., & Lin, R. 2009, ApJ, 691, 806
Lemaire, J., & Stegen, K. 2016, SoPh, 291, 3659
Li, B., Robinson, P. A., & Cairns, I. H. 2006, PhRvL, 96, 145005
Lin, R. 2011, SSRv, 159, 421
Lin, R., Evans, L., & Fainberg, J. 1973, ApL, 14, 191
Lin, R., Potter, D., Gurnett, D., & Scarf, F. 1981, ApJ, 251, 364
McClements, K. 1992a, A&A, 253, 261
McClements, K. 1992b, A&A, 258, 542
Mercier, C., & Rosenberg, H. 1974, SoPh, 39, 193
Morimoto, M. 1961, PASJ, 13, 285
Pierrard, V., Lazar, M., & Schlickeiser, R. 2011, SoPh, 269, 421
Reid, H. A., & Kontar, E. P. 2013, SoPh, 285, 217
Reid, H. A., & Kontar, E. P. 2018a, A&A, 614, A69
Reid, H. A., & Kontar, E. P. 2018b, ApJ, 867, 158
Reid, H. A., Vilmer, N., & Kontar, E. P. 2011, A&A, 529, A66
Reid, H. A. S., & Ratcliffe, H. 2014, RAA, 14, 773
Saint-Hilaire, P., Vilmer, N., & Kerdraon, A. 2012, ApJ, 762, 60
Schlickeiser, R. 1989, ApJ, 336, 243
Smith, H. M., Marsch, E., & Helander, P. 2012, ApJ, 753, 31
Sone, Y., & Sugimoto, H. 1993, PhFlA, 5, 1491
Steinacker, J., & Miller, J. A. 1992, ApJ, 393, 764
Tang, B., Che, H., & Zank, G. P. 2023, JPhCS, 2544, 012004
Tang, B., Zank, G. P., & Kolobov, V. I. 2020, ApJ, 892, 95
Tang, B., Zank, G. P., & Kolobov, V. I. 2022, ApJ, 924, 113
Thejappa, G., Gopalswamy, N., & Kundu, M. 1990, SoPh, 127, 165
Wild, J., & McCready, L. 1950, AusRA, 3, 387
Zank, G., Le Roux, J., Webb, G., Dosch, A., & Khabarova, O. 2014, ApJ, 797, 28
Zank, G. P. 2014, Transport Processes in Space Physics and Astrophysics: Lecture Notes in Physics, Vol. 877 (Berlin: Springer)
Zharkova, V. V., Arzner, K., Benz, A. O., et al. 2011, SSRv, 159, 357